3.11 ASSIMILATION OF SIMULATED CASA RADAR DATA OF VARIED STORM TYPES USING ENSRF FOR CONVECTIVE STORM ANALYSES AND FORECASTS

Elaine S. Godfrey*, Kelvin Droegemeier, Ming Xue, and Mingjing Tong
School of Meteorology and Center for Analysis and Prediction of Storms
University of Oklahoma, Norman, Oklahoma

1. INTRODUCTION

1.1 *Numerical weather prediction*

Although the dynamical equations governing the atmosphere have been known for nearly two centuries, it was not until the advent of digital computers that it became possible to use these equations in numerical models to produce useful forecasts. As computing power increases, the forecasting ability (both in time and space) from such models also increases, and their three-dimensional grid spacing significantly decreases. With the use of supercomputers, it is now possible to create 24-hour forecasts for most of the continental United States in a few hours using 2–4 km horizontal grid spacing. For example, Kain et al. (2004, 2005) performed such model runs and initiated them by interpolating the analysis state from the operational Eta model (Black 1994; Janjić 1994) with 12–40 km horizontal grid spacing to finer model grid spacing. However, defining the initial conditions only from a coarser grid analysis is not optimal and likely handicaps model performance in certain cases. For example, a coarser grid will likely not capture small-scale features such as gust fronts that can be extremely important for storm-scale numerical weather prediction.

Conventional data from surface observations, rawinsondes, and other instruments also are not available for model initialization or updates at or even near the same resolution as a convective storm model. As computing capabilities increase, data from denser observation networks such as radar are being used to initialize and update storm-scale numerical models. The assimilation of radar data in numerical models does come with a limitation: most of the model state variables (i.e., temperature, pressure, moisture, and condensate) are not observed directly by radar; only radial velocity and reflectivity are measured[1]. Thus, more advanced techniques are needed to retrieve quantities that are not directly observed.

Models that use adjoint techniques, such as 4D-Var, have been very successful at retrieving initial conditions and assimilating radial velocity and/or reflectivity data into forecast models (e.g., Sun and Crook 1997; Gao et al. 1998), but the adjoint code is computationally expensive to develop and maintain (TX05). Also, the 4D-Var approach requires significant effort in designing the background error covariance model. Alternatively, the recently-developed ensemble Kalman filter (EnKF) technique for assimilating radar data is much simpler to implement (Lorenc 2003). EnKF is growing in popularity for this reason; several studies of radar data assimilation with this method have been published in the past few years (Snyder and Zhang 2003; Dowell et al. 2004; Zhang et al. 2004; Caya et al. 2005; Tong and Xue 2005; Xue et al. 2006; Charron et al. 2006), and many more likely are underway.

At this time, the full assimilation and forecast cycles for a large number of ensemble members can take several days to execute on a supercomputing system, and are therefore not yet possible in real-time. However, as computing resources evolve, real-time radar data assimilation with high-resolution numerical models will become feasible, likely within the next several years. The resulting high spatial- and temporal-resolution short-range forecasts could assist weather forecasters, government entities, emergency managers, and private industry with warnings and weather-related decision-making.

1.2 *CASA radar network*

The National Science Foundation established the Engineering Research Center for Collaborative Adaptive Sensing of the Atmosphere (CASA) in September 2003 to develop low-power, low-cost solid-state Doppler radars for high-resolution sensing of the lower atmosphere. Unlike the existing WSR-88D radar network that scans the atmosphere in regular pre-set patterns, the CASA radars will be able to adapt to changing weather conditions and end user needs, and will operate collaboratively by coordinated directing of multiple radar beams.

The National Weather Service WSR-88D Doppler radars have limited sampling capabilities in the lower troposphere due to the curvature of Earth. Thus, meteorological conditions in the lowest three kilometers are grossly under-sampled, limiting the data available to initialize model forecasts in the region where storms develop.

The first Integrative Project (IP1) test bed of CASA X-band radars was installed in southwest Oklahoma in spring 2006. To keep installation costs manageable, some of the CASA radars were placed on existing communication towers having large data transmission capabilities and others were placed on newly constructed

[1] Velocity spectrum width is also available but is not as useful for numerical weather prediction.

* *Corresponding author address:* Elaine S. Godfrey, University of Oklahoma, School of Meteorology, National Weather Center, Suite 5900, 120 David L. Boren Blvd., Norman, OK 73072-7307 e-mail: esavageau@ou.edu.

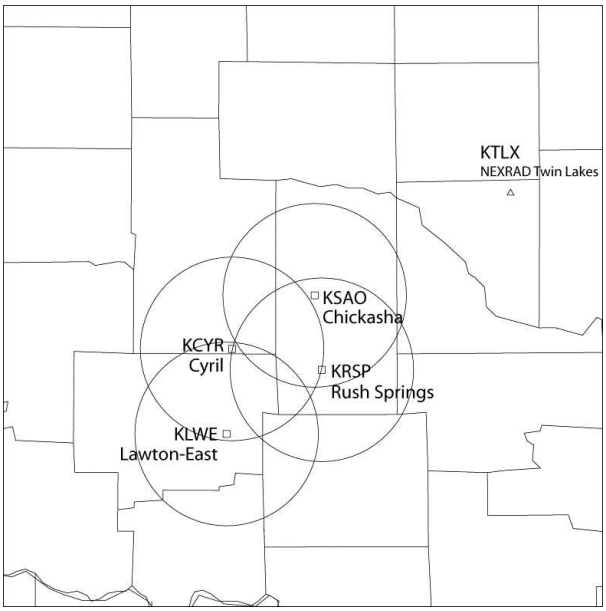

FIG. 1. Four-radar network for initial CASA deployment and the location of KTLX in central Oklahoma. Circles denote the anticipated 30-km radar range of the CASA radars.

short towers for easy access. Figure 1 shows the location of the IP1 network. Although real-time CASA radar data from this new network are not yet available, the effects of the CASA network on numerical weather prediction can be examined using simulated radar data.

1.3 *Goals of the study*

This study conducts a set of observation system simulation experiments (OSSEs) to assess the potential effects of assimilating simulated radar data using the ensemble square root Kalman filter (EnSRF) applied to storm-scale numerical weather prediction. Dynamically adaptive scanning strategies are unique to CASA, and the integration of adaptive radar observations using the EnSRF will be unique to this inquiry.

This work is part of an ongoing project which seeks answers to the following questions:

- Will the EnSRF technique work as well with different types of convection, such as multi-cell storms and quasi-linear convective systems, as it did with isolated supercells?
- What is the effectiveness of assimilating adaptively scanned data compared to data from conventional full volume scans?
- What are the most effective adaptive scanning strategies for use with the EnSRF? Do these vary by storm type, and if so, how?

To answer these questions, the EnSRF technique will be used to assimilate simulated radar data from multiple storm types, including a supercell and a multi-cell system. Further tests in this study will determine the effects of assimilating radar data from multiple scanning strategies of these and possibly other types of convection and will establish the most effective scanning strategy for each storm type. If plausible, adaptive scanning strategy recommendations based on the successful trials will be made for future use with the CASA testbed. Eventual simulations of larger storm systems using an expanded 9-node CASA radar network will reveal the utility of this larger system for storm-scale numerical weather prediction of multiple storm types.

2. HISTORICAL REVIEW

2.1 *Overview of ensemble-based prediction and data assimilation*

It is helpful to have an estimate of forecast skill in order to assess the potential usefulness of a particular forecast. The prediction of forecast skill is based on the theory of predictability (Wobus and Kalnay, 1995). Lorenz (1963) suggested that the future state of a stable dynamical system will remain arbitrarily close to its past history and will be quasi-periodic (and thus predictable), but that if all states are unstable, there is a finite limit of predictability. The atmosphere is certainly not stable, observations are not perfect, and the solutions to its nonperiodic flow are only readily determined by numerical procedures (Lorenz 1963). Many years later, Lorenz (1996) assumed that the predictions of individual chaotic dynamical systems, such as the atmosphere, would be error-free if the initial state could be observed without error and the extrapolation procedure is error-free, which is impossible if the governing laws involve any randomness (which they do).

So what is to be done? If the amount of uncertainty in the initial state is known or can be estimated, then it is possible to perturb the initial state proportional to the known or estimated uncertainty in order to generate a group, or ensemble, of forecasts. Leith (1974) was the first to use such "Monte Carlo" experiments, randomly generating the perturbed errors that were based on analysis uncertainty. He showed that even a small number of forecast ensemble members (i.e., ten members) could improve the skill of the mean forecast (and is appreciably better than a conventional single forecast) and could be used to provide error estimates.

So what is considered to be an ensemble forecast? Do forecasts from two or more unique models constitute an ensemble? What about forecasts from the same model with perturbed initial conditions? Sivillo et al. (1997) defined an ensemble forecast to be "a collection of two or more forecasts that verify at the same time," which would include both of the previous examples. When appropriate, it is possible to weigh the individual members of the ensemble according to their respective ages, resolution, model accuracy, and other relevant factors to minimize the root-mean-square forecast error (Van den

Dool and Rukhovets 1994). As to the purpose of ensemble forecasting, Sivillo et al. (1997) defined it as the recognition of "the inherent uncertainty of weather forecasting," and suggested that its goals are "to increase the average forecast accuracy, to estimate the likelihood of various events, and to estimate the decay of forecast skill with increasing lead time." The authors also asserted that the largest value for ensemble forecasting is found in the more general case when non-linear processes influence forecast errors.

As Leith (1974) and many others have demonstrated (e.g., Elmore et al. 2002, 2003; Kong et al. 2006a,b), an ensemble of forecasts can be used to create a single forecast, and it can also be used to glean additional information in addition to a simple average. For example, the individual members of an ensemble forecast can suggest additional possibilities outside the mean, the probabilities of which can be estimated (Anderson 1996), although these probabilities may need to be corrected due to an underestimation of the range of possibilities (i.e., an ensemble model won't forecast a record high) (Hamill and Colucci 1997a; Zhu et al. 1996; Buizza 1997). Wobus and Kalnay (1995) suggested that an ensemble of forecasts could also be used to predict the skill of probability forecasts. Lastly, an ensemble of forecasts can suggest locations for additional special observations that would improve forecast accuracy (Bishop and Toth 1996; Emanuel et al. 1996, Morss et al. 2001).

Although ensemble forecasting has these many advantages, it is computationally expensive, and a tradeoff must be made among between model initialization, model complexity, the number of forecasts in the ensemble, and the amount of computer and human time needed to process the information due to computer limitations and time constraints (Sivillo et al. 1997).

2.2 *Overview of the ensemble Kalman filter*

The use of a Kalman filter with an ensemble of forecasts started by randomly-perturbed initial background states was first introduced by Evensen (1994), and has gained popularity in recent years due to its ease of use and relatively affordable computational requirements. This new technique, previously called the 'Monte Carlo' method and later dubbed EnKF, uses a large number of randomly distributed points in phase space that represent a specific probability distribution function (PDF), which are integrated forward in time. These forecasts can be used to calculate estimates for moments of the PDF at different times, and the errors in the solution PDF will approach zero at a rate proportional to $N^{-0.5}$, where N is the number of ensemble members (Evensen 1994). Essentially, this technique is a way to approximate the evolution of the error statistics. Evensen (1994) proved that use of the EnKF technique eliminated the unbounded error growth found in the extended Kalman filter. Houtekamer and Mitchell (1998) first implemented the stochastic method, which treats observations as random variables that are subject to additional perturbations such that the analysis error covariance is consistent with that of the traditional Kalman filter, followed shortly by Burgers et al. (1998), Houtekamer and Mitchell (2001), Evenson (2003), and others. Houtekamer and Mitchell (1998) also introduced a cutoff radius, which is now commonly known as the covariance localization radius, beyond which the covariance between variables is assumed to be zero.

Since the introduction of the EnKF, many new forms of this technique have been developed. Hamill and Snyder (2000) developed a hybrid ensemble Kalman filter/3D-variational (3D-Var) analysis scheme. In it, the background error covariance is a weighted average of the static 3D-Var error covariance and the time evolving EnKF error covariance, and the state estimate is computed using the 3D-Var algorithm. The authors found that the analysis performed best when the EnKF background error covariance was given almost full weight, especially for large ensembles. However, lower covariance weighting was found to be desirable for smaller ensemble sizes. As expected, the error decreased with the use of larger ensembles. Bishop et al. (2001) developed the Ensemble Transform Kalman Filter (ETKF), in which the error statistics predicted by the ensemble were used to determine the optimal configuration of future targeted observations. The ETKF was tested using OSSEs (Bishop et al. 2001), and the authors found that it provides direct observation sensitivity. Anderson (2001) developed a method known as the Ensemble Adjustment Kalman Filter (EAKF), where the observations are not perturbed. The resulting ensemble mean is still correct, but the variance is too low, so a linear operator is derived to replace the traditional gain matrix. Unfortunately, the measurement covariance matrix is required to be inverted when it is not a diagonal matrix. This is true for all EnKF methods. Further examples of the use of EnKF can be found in Evensen (2003).

2.3 *Overview of the ensemble Kalman square-root filter*

Whitaker and Hamill (2002, hereafter WH02) developed the deterministic EnSRF to better estimate the analysis variance by avoiding sampling errors associated with the use of perturbed observations. The ensemble mean and deviations from the mean are updated separately such that the ensemble mean analysis and the analysis covariance are consistent with that predicted by Kalman filter theory. The EnSRF, like the stochastic EnKF, assimilates the observations into the model's initial conditions and processes them sequentially. This sequential processing avoids storing and manipulating very large matrices when solving the Kalman filter equations by reducing both the observation-error covariance matrix and the background error covariance matrix between observation points to scalars (WH02). One drawback of the sequential processing of observations is the difficulty in

parallelizing the ensemble members, the lack of which is impractical for many types of observations (Lorenc 2003). However, the analysis error from EnSRF experiments is likely to be less than the error from EnKF experiments due to the underestimation of error covariance that is present in EnKF as a result of the perturbed observations (WH02). According to WH02, the EnSRF is conceptually simpler than and just as fast as the EnKF, and possibly more accurate than the EnKF for a given ensemble size. The authors tested and found that the ensemble mean error from the EnSRF analysis of a general circulation model is lower than that of the EnKF analysis for the same ensemble size. Thus, there are substantial benefits from using a data assimilation system that does not require perturbed observations.

2.4 *Formulation of the ensemble Kalman square-root filter*

After the notation of Ide et al. (1997) and WH02, let the superscripts a, b, and o denote analysis, background, and observation, respectively. Then x^b is an m-dimensional background model forecast state vector, y^o is a set of observations with p dimensions, $\mathbf{H}$ is the linearized version of the observation operator, H, which projects state variable x to observation y^o, $\mathbf{P}^b$ is the background or prior error covariance matrix with $m \times m$-dimensions, $\mathbf{R}$ is the $p \times p$-dimensional observation-error covariance matrix, and x^a is the minimum error-variance estimate of the analyzed state that is given by Lorenc's (1986) Kalman filter equation:

$$x^a = x^b + \mathbf{K}(y^o - \mathbf{H}x^b), \tag{1}$$

where the Kalman gain matrix, $\mathbf{K}$, is given by:

$$\mathbf{K} = \mathbf{P}^b\mathbf{H}^T(\mathbf{H}\mathbf{P}^b\mathbf{H}^T + \mathbf{R})^{-1}. \tag{2}$$

The analysis equations for the ensemble-mean state $\overline{x}$ and the deviation from the mean for the ith member of the ensemble $x_i^{'a}$ are given by

$$\overline{x}^a = \overline{x}^b + \mathbf{K}(\overline{y}^o - \mathbf{H}\overline{x}^b) \tag{3}$$

and

$$x_i^{'a} = x_i^{'b} + \widetilde{\mathbf{K}}(y^{'o} - \mathbf{H}x_i^{'b}), \tag{4}$$

respectively. Here, the background analysis-error covariance $\mathbf{P}^b$ is given by:

$$\mathbf{P}^b = \overline{x^{'b}x^{'bT}} \equiv \frac{1}{n-1}\sum_{i=1}^{n} x^{'b}x^{'bT}, \tag{5}$$

where n is the ensemble size, $\mathbf{K}$ is the traditional Kalman gain matrix in Eq. (2), and $\widetilde{\mathbf{K}}$, is the gain function used to update deviations from the ensemble mean (WH02).

Equation (4) can be simplified to the following:

$$x^{'a} = x^{'b} - \widetilde{\mathbf{K}}\mathbf{H}x^{'b} = (I - \widetilde{\mathbf{K}}\mathbf{H})x^{'b}. \tag{6}$$

For individual observations that are assimilated one at a time, the background error covariance matrix between observation points, $\mathbf{H}\mathbf{P}^f\mathbf{H}^T$, and the observation error covariance matrix, $\mathbf{R}$, are scalars, and $\mathbf{K} = \alpha\widetilde{\mathbf{K}}$, with

$$\alpha = \left(1 + \sqrt{\frac{\mathbf{R}}{\mathbf{H}\mathbf{P}^b\mathbf{H}^T + \mathbf{R}}}\right)^{-1}. \tag{7}$$

After Xue et al. 2006 (hereafter XTD06), a covariance inflation procedure is necessary due to the frequent underestimation of the background error covariance that is a result of the limited size of the ensemble (Anderson 2001). When the ensemble square-root Kalman filter is used, Equation 6 can be modified with the addition of a covariance inflation factor (usually slightly larger than one), β:

$$x_i^{'a} = \beta(I - \alpha\mathbf{K}\mathbf{H})x_i^{'b} \tag{8}$$

(XTD06).

In the EnSRF, the ensemble mean and the departures are independently updated and the observations are unperturbed, which requires no additional computational time than the traditional EnKF with perturbed observations (WH02).

2.5 *Previous work using radar data and the EnKF/EnSRF methods*

With the growing success and popularity of the EnKF and EnSRF and increasing computing capabilities, it was only a brief time from their development before radar data were assimilated into storm-scale models using these techniques. Snyder and Zhang (2003) were the first to use the EnKF technique to assimilate simulated single-Doppler radar observations into a numerical cloud model, and obtained promising results. The authors simulated a supercell by introducing a warm bubble into a homogeneous environment characterized by the 0000 UTC 25 May 1977 Del City composite sounding. Snyder and Zhang (2003) assimilated simulated radial velocity data into the model and successfully estimated the unmeasured quantities of vertical velocity and temperature in the analyses. The authors also found that the analysis quality is affected by covariances between V_r and T, q, and condensate as well as the initialization chosen for the ensemble members prior to assimilating the first observations.

Continuing this work, Zhang et al. (2004) again used a five-minute radar observation assimilation period. The authors used different depths of radial velocity data and found that the lowest data aided the capture of the detailed cold pool structure, but runs without these low-level observations performed comparably to runs with all levels of data when given a longer assimilation period. The model also successfully captured the supercell structure when only the V_r data below four kilometers were assimilated. However, using radar observations only above four kilometers failed to properly assimilate

the storm unless surface temperature and wind observations from a hypothetical surface mesonet were included. Zhang et al. (2004) also tested the effects of 2-minute assimilation cycles, and found minimal effect after the first few cycles.

Dowell et al. (2004) were the first to assimilate real radar observations into a numerical storm-scale model using EnKF. The authors assimilated both V_r and Z, and the results from the EnKF analyses were compared to observations from another radar, dual-Doppler wind syntheses, and tower *in situ* measurements. Not surprisingly, Dowell et al. (2004) found that the large observational errors present in real data make assessment more difficult than for the relatively clean simulated radar data. Overall, the results were successful, with a few drawbacks. The scientists found that the magnitudes of the vertical velocity and vertical vorticity were similar to the dual-Doppler analyses, with the exception of a stronger low-level updraft in the EnKF analyses. The low-level temperature EnKF analyses performed poorly, partially due to the warm-rain microphysical scheme used in the model and partly due to the limitations of the observation system. The Doppler data that was assimilated did little to correct temperature errors in the low-level cold pool, which was too strong in the EnKF analyses (Dowell et al 2004). The authors also tested a two kilometer radius of influence of observations, which produced poor results. Thus, a larger radius of influence and an ice microphysical scheme may help solve some of the issues with the cold pool. However, the authors noted that, "since the evolution of convection over periods of tens of minutes depends significantly on cold pools, the implications for operational numerical forecasting of convection are discouraging if cold pools cannot be predicted well by the model, and assimilation of Doppler observations cannot correct the model trajectory" (Dowell et al. 2004). Thus, additional observations that can better capture this feature are needed.

More recently, Charron et al. (2006) assimilated radial velocity data from nine simulated radars using an EnKF using a larger time and length scales than previous works. The simulated data were assimilated into a nonhydrostatic Boussinesq model with horizontal dimensions of 1000×1000 km every thirty minutes over a four-day assimilation period. The model successfully analyzed the horizontal winds and temperature over a four day period, but did not successfully resolve the vertical velocity, likely due to the type of data assimilated and the localization radius. Their results indicated that the EnKF technique with radar data could perform well in the mesoscale range, and the authors suggested that results could be more accurate if a hydrostatic model were used.

Previous studies at the University of Oklahoma have successfully used the EnKF and EnSRF techniques for the assimilation of simulated single- and multiple-Doppler radar data of modeled convective storms into the initial conditions of a numerical storm-scale model (Tong and Xue 2005, hereafter TX05; XTD06). These studies have demonstrated encouraging results in retrieving the model state variables (i.e., u, v, w, p, θ, q_v, etc.) with the use of a multi-class ice microphysical scheme. The model state variables were then successfully implemented into simulated supercell storms using the EnKF and EnSRF techniques (TX05, XTD06). TX05 found that the best results are obtained when both radial velocity and reflectivity data from the radar emulators are assimilated into the model. The authors also showed that the inclusion of simulated CASA and WSR-88D radar data from an isolated supercell storm into ARPS improved the forecast over that using WSR-88D radar data alone. TX05 also showed that dynamically consistent background error covariances develop in the system, most notably in the later cycles, even when velocity data and data outside of the precipitation regions are not assimilated. Thus, the authors concluded that such flow-dependent background error covariances play a crucial role in successful data assimilation and retrieval (XTD06).

Of the previous radar assimilation work using the EnKF or EnSRF, no one has yet studied the impact of assimilating data from a multi-cell storm system. Additionally, the effects of assimilating adaptive radar data into a model using the EnSRF technique have not yet been evaluated. This ongoing project is a continuation of the work begun by TX05 and XTD06, and extends their model to develop a quasi-realistic multicell simulation and supercell simulation that can be adaptively sampled using an altered radar emulator and reproduced using the EnSRF technique. The effects of short and long assimilation time scales, an adaptive radar network, and different adaptive scanning strategies will be evaluated in this endeavor.

3. NUMERICAL MODEL OSSE CONFIGURATIONS

3.1 *ARPS prediction model*

The Center for Analysis and Prediction of Storms (CAPS) at the University of Oklahoma developed the ARPS, a fully compressible and nonhydrostatic atmospheric prediction system that has been well documented in previous literature (Xue et al. 2000, 2001, 2003), and has a demonstrated ability to create multiple types of convective storm systems (Nascimento and Droegemeier 2002; TX05; Richardson et al. 2006).

ARPS is used here as a three-dimensional cloud model and contains twelve prognostic state variables, including the three-dimensional wind components u, v, and w, potential temperature θ, pressure p, the mixing ratios for snow q_s, hail q_h, cloud water q_c, rainwater q_r, and cloud ice q_i, the water vapor specific humidity q_v, plus the turbulence kinetic energy used by the 1.5-order subgrid-scale turbulence closure scheme (Stull 1988; XTD06). The modified six-category water/ice scheme of Lin et al. (1983) parameterizes the microphysical processes,

and the implementation of this scheme follows that of Tao and Simpson (1993). This scheme assumes that all ice particles are spherical and it assumes an exponential particle size distribution function for rain, snow, and hail/graupel (Xue et al. 2000). Because the simulation domain is relatively small, is over flat terrain, and is over a brief time scale, the terrain and Coriolis options are turned off.

3.2 *Radar emulator*

Although the CASA radar network is still undergoing testing and data are not yet available in real time, the potential effects of this radar network can still be estimated using OSSEs. More importantly, conducting EnSRF experiments with simulated adaptive scanning strategies will produce estimates of the effectiveness of these strategies and will determine optimal scanning strategies of different storm types for numerical weather prediction purposes.

One existing WSR-88D radar in central Oklahoma, Twin Lakes (KTLX), and up to four CASA test-bed radars that were recently installed in central Oklahoma are simulated in this study. The WSR-88D radar has a 10 cm wavelength, a 1° beam width, a total of 14 elevations with the lowest elevation at 0.5° and highest at 19.5°, and a radial resolution of 250 m for radial velocity and 1 km for reflectivity. The maximum range is set at 230 km, which is sufficient to cover the entire model domain (i.e., Figure 3). The four radars in the IP1 CASA test-bed have a three centimeter wavelength (X-band), a 2° beam width, and an assumed maximum range of 30 km. The CASA radars in the Oklahoma test-bed were installed in the spring of 2006 near Chickasha, Rush Springs, Lawton, and Cyril in southwestern Oklahoma. These radars will be about 90 km to the southwest of KTLX, and are shown in Figure 1 with their expected 30 km range rings.

To generate the simulated radar data, a storm system must first be created. This is called the truth or reference simulation. The truth simulation is established by placing one or more warm thermal perturbations in a horizontally homogenous background state that is typically characterized by an observed or idealized sounding. This warm bubble will rise and initiate an updraft, which will evolve into one or more storms in the three-dimensional model. Once the storm has developed far enough to generate precipitation, a radar emulator 'examines' the model output from the truth simulation and assigns simulated reflectivity and radial velocity values to different locations based on the amount of reflective targets in the area and their respective motions. In the EnSRF technique, an ensemble of initial model states is created by perturbing the background state with Gaussian-distributed perturbations. The ensemble of forecasts runs independently for a brief period (generally five minutes), then the observations are assimilated and the model states are corrected accordingly. This forecast and assimilation cycle is repeated for a moderate length of time, generally until the ensemble mean error is reasonably low, and then a medium-term forecast is usually run without observation corrections.

For these OSSEs, the prediction model (which produces the truth simulation) and the observation operators are assumed to be without error, which is a common assumption in OSSE studies. This study uses the radar emulator and EnSRF procedure developed by TX05, XTD06, and Tong (2006). Following their work, standard precipitation-mode parameters for CASA radars are assumed and a volume scan consists of ten elevation scans 2° apart, beginning at 1° elevation. After XTD06, the emulated radar data are assumed to be on the original radar elevation angles and then interpolated from the radar polar coordinate to the Cartesian coordinate system. Since the emulated radar observations are not yet at the model grid points, a forward observation operator is used to adjust the data from the model's vertical levels to the elevation levels that would be seen by a radar on the surface. The radar emulator performs power-gain-based sampling in the vertical direction using

$$\varphi_e = \frac{\sum G\varphi_g \Delta z}{\sum G \Delta z}, \tag{9}$$

where φ_e and φ_g are the elevation level, e, and grid point values, g, of either radial velocity (V_r) or reflectivity (Z), and Δz is the depth of the layer in which φ_g resides. The power gain function, G, is assumed to be Gaussian and has the form

$$G = \exp\left[-4\ln 4(\frac{\phi_g - \phi_0}{\phi_w})^2\right], \tag{10}$$

following Wood and Brown (1997), where ϕ_w is the beam width, ϕ_g is the elevation angle for the grid point value, and ϕ_0 is the elevation angle at the beam center.

To calculate radial velocity, the grid point values involved in the numerator of Equation 9 are first calculated from

$$V_{rg} = u\cos\phi_g \sin\gamma_g + \nu\cos\phi_g\cos\gamma_g + w\sin\phi_g, \tag{11}$$

where subscript g denotes the grid point value, ϕ_g is the *local* elevation angle defined earlier, γ_g is the azimuth angle of the radar beam that goes through the given grid point, and u, v, and w are the velocities of the model which are interpolated to the scalar point of a staggered Arakawa C-grid (Arakawa and Lamb 1977; XTD06). Hydrometeor sedimentation effects are not involved in the data or assimilation because the radial velocity is sampled directly from the velocity fields.

Simulated reflectivity, Z (dBZ), is calculated from rainwater, snow and hail hydrometeor mixing ratios with the same formulations as in TX05 and XTD06, and is formally given by

$$Z = Z(q_r, q_s, q_h), \tag{12}$$

where q_r, q_s, and q_h are rain, snow, and hail mixing ratios, respectively (Smith et al. 1975). These formulations are consistent with the Lin et al. (1983) ice microphysics scheme used in ARPS. Future work may include studying the effects of attenuation, which may have a significant effect on the CASA radar data.

After the radial velocity and reflectivity are sampled from the grid pointed data, observation errors are simulated by adding Gaussian random errors with zero mean and a standard deviation of 1 m s^{-1} and 5 dBZ for velocity and reflectivity, respectively. These simulated data are then interpolated from the radar polar coordinate to the Cartesian coordinate system and incorporated into ARPS using the EnSRF technique described above. It should be noted that no data are collected or assimilated where no grid level lies within the beam width, which serves to naturally thin the data at well-sampled low levels.

4. MULTICELL MODEL SIMULATIONS

4.1 *Environment*

The EnSRF code system developed by Mingjing Tong in conjunction with CAPS and the University of Oklahoma School of Meteorology for use with ARPS was used (TX05; XTD06; Tong 2006) in this study. In order to develop adaptive scanning strategies that may eventually be implemented when the CASA testbed is fully operational, it is important to have storm simulations that are realistic in their size, intensity and behavior. Droegemeier and Levit (1993) used ARPS to simulate supercells and multi-cell storm systems and found that the modeled multi-cell systems, which formed in weak-shear environments, were much more sensitive to the initial conditions than the supercell storms. Because of this sensitivity, it has taken many trials to develop a reasonably realistic and strong multi-cell simulation that lasts for four hours and can be successfully used with the EnSRF technique.

To establish a suitably unstable initial environment that was capable of generating a multi-cellular convective system, the vertical temperature, moisture, and wind-speed profile developed by Weisman and Klemp (1982, hereafter WK82) was added to ARPS (Richardson 1999). The environmental potential temperature $\overline{\theta}$ and relative humidity H are given by

$$\overline{\theta} = \begin{cases} \theta_0 + (\theta_{tr} - \theta_0)\left(\frac{z}{z_{tr}}\right)^{\frac{5}{4}}, & z \le z_{tr} \\ \theta_{tr} \exp\left[\frac{g}{c_p T_{tr}}(z - z_{tr})\right], & z > z_{tr} \end{cases}$$

and

$$H(z) = \begin{cases} 1 - \frac{3}{4}\left(\frac{z}{z_{tr}}\right)^{\frac{5}{4}}, & z \le z_{tr} \\ 0.25, & z > z_{tr} \end{cases}, \qquad (13)$$

where $z_{tr} = 12$ km, $\theta_{tr} = 343$ K, and $T_{tr} = 213$ K represent the height, potential temperature and actual temperature, respectively, at the tropopause, and $\theta_0 = 300$ K is the surface potential temperature (WK82). WK82 also developed the wind profile used here, which is given by

$$U = U_s \tanh\left(\frac{z}{z_s}\right), \qquad (14)$$

where $z_s = 3$ km and $U_s = 12$ m s^{-1} (after Richardson 1999).

To assess the effects of altering the vertical wind profile in both horizontal dimensions, a similar equation for the meridional wind profile in the vertical direction is included and is given by,

$$V = V_s \tanh\left(\frac{z}{z_s}\right), \qquad (15)$$

where $z_s = 3$ km and V_s is a constant set in the model. In order to approximate a well-mixed moist boundary layer that would be conducive to multi-cellular storm development, the mixing ratio near the surface is kept constant (Figure 2) at 16 g kg^{-1}. Several trials were conducted with $U_s = 12$ m s^{-1} and V_s set to either 2.5 m s^{-1} or 5.0 m s^{-1}.

4.2 *Truth simulation*

Multiple runs were necessary to establish a sufficiently realistic multicell system simulation, and the domain was set up such that the CASA radars had thorough coverage of the storms throughout the entire assimilation period. Several runs were executed before the proper

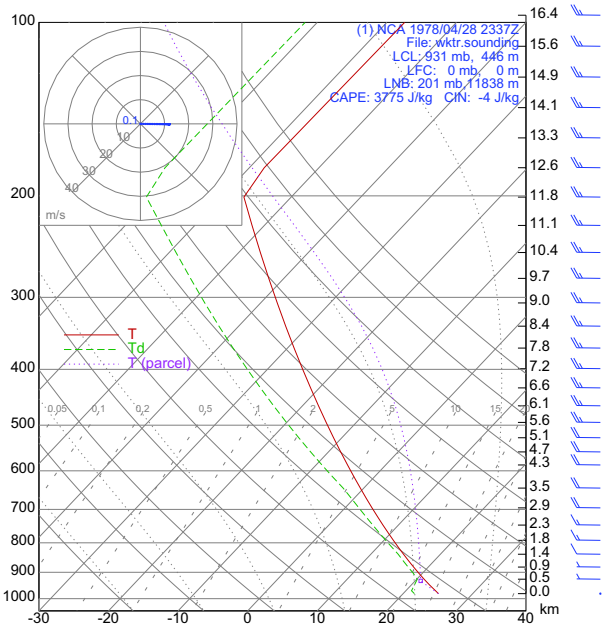

FIG. 2. Skew T-Log P diagram from the thermodynamic profile given by Weisman and Klemp (1982), using an surface mixing ratio value of 16 g kg^{-1}.

domain size and initial bubble location could be determined. ARPS has a provision for domain motion in which certain wind speeds in the x and y directions are subtracted from the environmental sounding, which allows manipulation of the domain such that storms remain away from the lateral boundaries. The addition of domain motion allowed a reduction of the necessarily large domain and reduced the computing time for each EnSRF run by several days. A constant wind of $u = 7$ m s^{-1} was subtracted from the observed sounding to maintain the storm within the domain.

This relatively steady multi-cell simulation was used as the truth simulation, and the radar emulator described above sampled the storms with full-volume snapshots along the radar elevation angles every 2.5 minutes. Observation errors were simulated by adding Gaussian random errors with zero mean and a standard deviation of 1 m s^{-1} and 5 dBZ for velocity and reflectivity, respectively. These data are then interpolated from the radar polar coordinate to the Cartesian coordinate system and imported back into ARPS using the EnKF technique described in Section **3.2**.

The storm simulations were initiated in a horizontally homogeneous atmosphere following the WK82 equations and parameters described in Section **4.1**, and contained two axially symmetric thermal perturbations, described below. The WK82 wind parameters for the zonal and meridional winds were set to $\overline{U}_s = 12$ m s^{-1}, and $\overline{V}_s = 2.5$ m s^{-1}, respectively. A two-second time step was used, and model conditions are output every five minutes to allow for five-minute volume scan simulations by the radar emulators. More details on the truth simulation initialization parameters are shown in Table 1.

The physical domain had dimensions of $96 \times 80 \times 20$ km in the x, y, and z directions, respectively, and a horizontal grid spacing of 1.0 km. Due to the relatively small domain size, the effects of the Coriolis force and Earth's curvature were neglected. To better resolve the lower atmosphere, the 40-layer vertical grid was stretched using a hyperbolic tangent function and had a minimum vertical resolution of 200 m at the surface. The domain is centered on the latitude and longitude coordinates (34.7767, -98.0331), shown in Figure 3, and covers much of the CASA radar domain.

The first bubble had a horizontal radius of 10 km and a vertical radius of 1500 m, and was initially centered on the point $x = 16$ km, $y = 64$ km, with the origin of the coordinate system in the southwest corner of the grid. In order to more quickly develop a multicell simulation, a second and slightly smaller warm and axially symmetric thermal perturbation was added to the initial time in the truth simulation. The temperature is increased 4°C at the center (located 1500m AGL) of each bubble and decreases gradually to the edges. The first bubble has a horizontal radius of 10 km and a vertical radius of 1500 m, and is initially centered on the point $x = 20$ km, $y = 30$ km, with the origin of the coordinate system in the southwest corner of the grid. The second bubble has a horizontal radius of 7 km, a vertical radius of 1050 m, and is initially centered on $x = 23$ km, $y = 50$ km, with the origin of the coordinate system in the southwest corner of the grid. The initial locations of the bubbles are chosen so that over most of the assimilation period, most of the multicell storm system remains within the domain.

The addition of a second bubble proved to be effective at generating multiple updrafts by the initiation of the first forecast cycle at 55 minutes, and these cells continued to evolve into a large multi-cellular thunderstorm complex with several strong vertical updrafts by two hours (Figure 4) and by three hours and forty minutes (Figure 5). The first forecast was initiated at 55 minutes, the first simulated radar data were assimilated at one hour, and the assimilation cycle continued ingesting data every five minutes for one hour. As before, both radial velocity and reflectivity were assimilated. To bet-

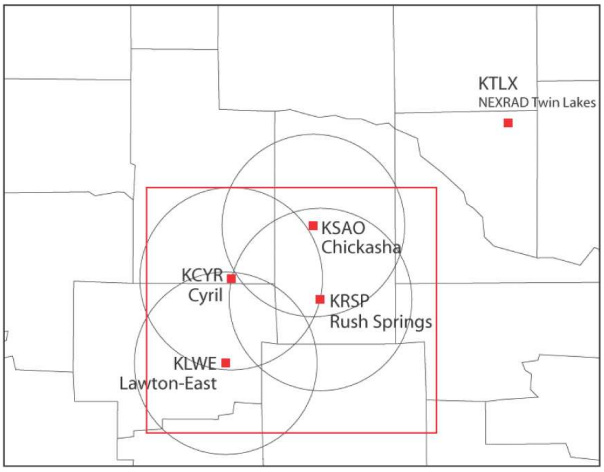

FIG. 3. The four-radar network for the initial CASA deployment and the location of KTLX in central Oklahoma. Circles denote the anticipated 30-km radar range, and the red box indicates the model domain.

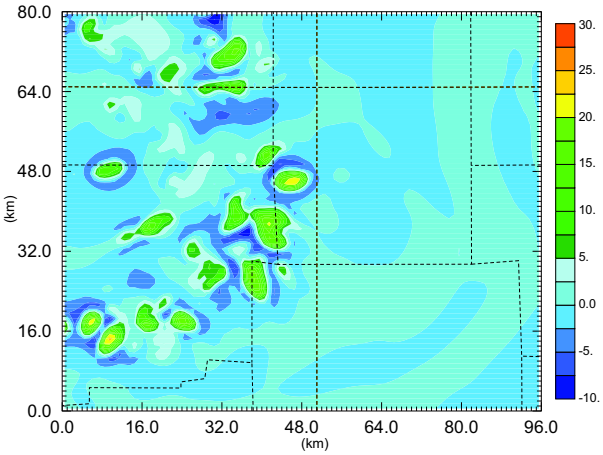

FIG. 4. Horizontal cross section of vertical velocity (m s^{-1}) at two hours at $z = 4.6$ km AGL.

TABLE 1. List of parameter settings for dual-bubble ARPS model simulations.

Parameters	Value
Horizontal grid spacing (array size)	1 km (96 × 80 points)
Vertical grid stretching function	Hyperbolic tangent
Vertical grid spacing (number of levels)	200 m – 800 m (40 levels)
Time step	2 sec
Coriolis and earth curvature effects	Not used
Fourth-order mixing coefficient	1×10^{-3} s^{-1} horizontal, 5×10^{-4} s^{-1} vertical
Pressure field de-trending	On
Nondimensional divergence damping coefficient	0.05
Rayleigh damping coefficient (applied above 12 km only)	0.05 s^{-1}
Lateral boundary conditions	Radiation (open)
Top & bottom boundary conditions	Rigid wall with upper sponge (wave absorbing layer)
Horizontal & vertical advection scheme	4$^{\text{th}}$-order horizontal, 2$^{\text{d}}$-order vertical with leapfrog time step
Cumulus parameterization	Not used
Grid-scale microphysics	6-category water/ice microphysics of Lin et al. (1983)
Turbulence parameterization	1.5-order TKE closure
Sub-grid scale turbulence	Isotropic
Radiation parameterization	Not used
Land surface and vegetation scheme	Not used
Computational mixing	4$^{\text{th}}$-order in horizontal, 4$^{\text{th}}$-order in vertical
Horizontal and vertical wind perturbations, standard deviations	1.0 – 1.5 m s^{-1}
Potential temperature perturbation, standard deviations	1.5 K
Water vapor mixing ratio perturbation, standard deviations	0.0002 – 0.0005 g kg^{-1}
Other mixing ratio perturbations, standard deviations	0.0002 – 0.0005 g kg^{-1}
Horizontal radius of influence	4 – 6 km
Zonal grid translation	6 m s^{-1}
Surface mixing ratio for WK82 profile	16 g kg^{-1}
WK82 wind parameters for the zonal and meridional winds	$\overline{U}_s = 12$ m s^{-1}, and $\overline{V}_s = 2.5$ m s^{-1}
Covariance inflation	10-25% when $Z > 10$ dBZ
CASA radar cutoff elevation	3 km

ter represent the actual CASA data that will be assimilated in future projects, the emulated radar data were cut off at 3 km above ground level. The removal of data above this height had little/no negative effect on the three-dimensional RMS error, and very slightly increased the ensemble spread. Attenuation, which can play a significant role in data from X-band radars, was not accounted for in these trials but will be included in future simulations.

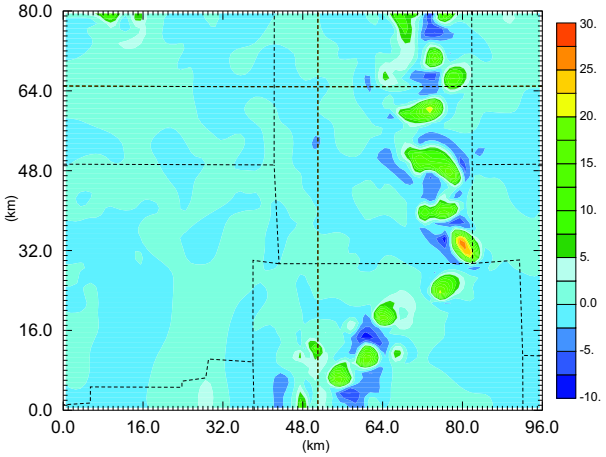

FIG. 5. Horizontal cross section of vertical velocity (m s^{-1}) at 3 hours 40 minutes at $z = 4.6$ km AGL.

4.3 *EnSRF results with 5-minute assimilation cycles*

A covariance inflation procedure is necessary due to the frequent underestimation of the background error covariance that is a result of the limited size of the ensemble. Although based on the work of Anderson (2001), this inflation will only be applied at the grid points where the observations with $Z > 10$ dBZ are of direct influence, instead of being applied to the entire domain. Otherwise, spurious convection would be a significant problem outside regions of observed precipitation. Due to the large amount of data ingested into the model, the ensemble spread was relatively low, so a covariance inflation of 10-25% was added to different ensemble runs. This boosted the ensemble spread, but increasing the covariance inflation too much (i.e., 25%) can lead to runs where the spread actually increases with time during the assimilation period. This effect is amplified in cases where less data are ingested, such as when a smaller radius of influence is used (Figure 6). Additionally, the horizontal and vertical localization radii were tuned to find the optimal combination of increasing the spread and decreasing the RMS error. A small radius of influence will increase the spread to more optimal levels, but it will also increase the three-dimensional RMS error. Thus, an appropriate balance must be found. The radii coincident with the lowest RMS errors with 25% covariance inflation and low initial perturbations are the relatively large values of 6 km in both the horizontal and vertical directions. The lowest 3-D RMS error for u at the end of the one-hour assimilation cycle is 1.5 m s^{-1}, and the lowest for v was 1.9 m s^{-1} (Figure 7).

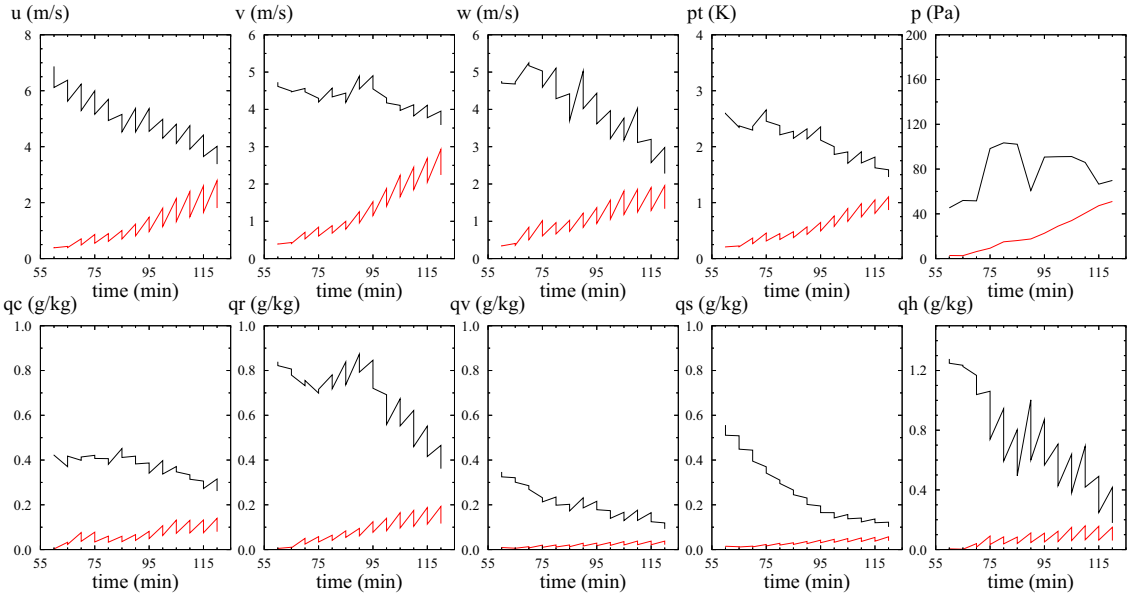

FIG. 6. The three-dimensional root mean square (RMS) error plots for the EnSRF multicell simulations that assimilated in radar data from both KTLX and all four CASA radars. The black lines denote the RMS error from the run, and the red lines indicate the spread across the forty-member ensemble. This particular run used 25% covariance inflation and had a four kilometer horizontal and vertical radius of influence.

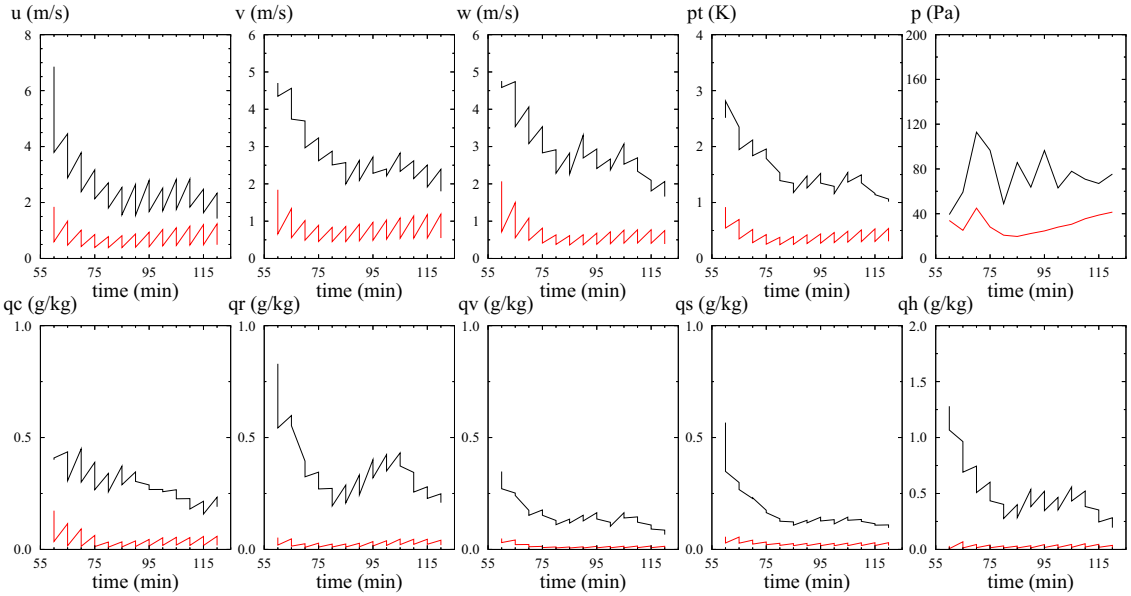

FIG. 7. As in Figure 6, but for a multicell simulation that used 25% covariance inflation and a six kilometer horizontal and vertical radius of influence.

The background state variables were randomly perturbed such that the standard deviations of the winds were 1.0 m s^{-1} for each direction and those of the microphysical variables were 0.0002 g kg^{-1} for each variable. In most of the trial runs, a smoothing filter was applied to the perturbed background state, which helped decrease the RMS error considerably. To compare the effects of larger initial perturbations, a simulation with the standard deviation of the initial wind perturbations of 1.5 m s^{-1} and microphysical variable perturbations with a standard deviation of 0.0005 g kg^{-1} had significantly higher RMS error values–about twice that of comparable runs (Figure 8). The initially perturbed background state negatively impacts the various small storms in the unstable multi-cell environment more than the supercell simulations. This is likely due to the weak and transient nature of the individual members of the multicell system, which are not as robust as the isolated supercell. More-

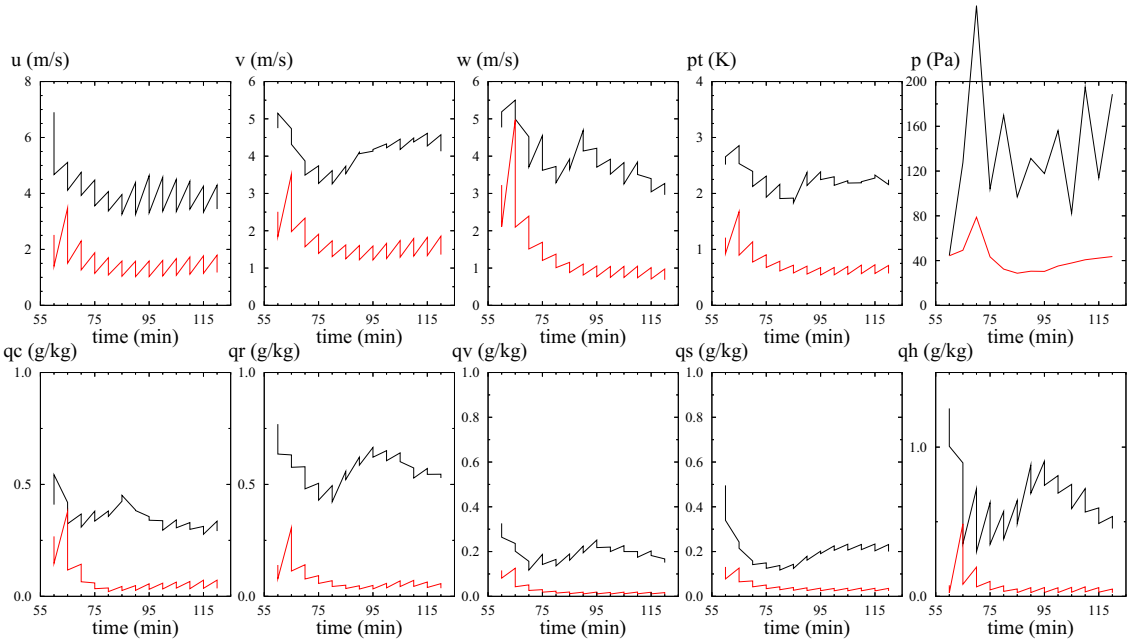

FIG. 8. As in Figure 6, except with higher initial background perturbations, 10% covariance inflation, and a 5 km radius of influence.

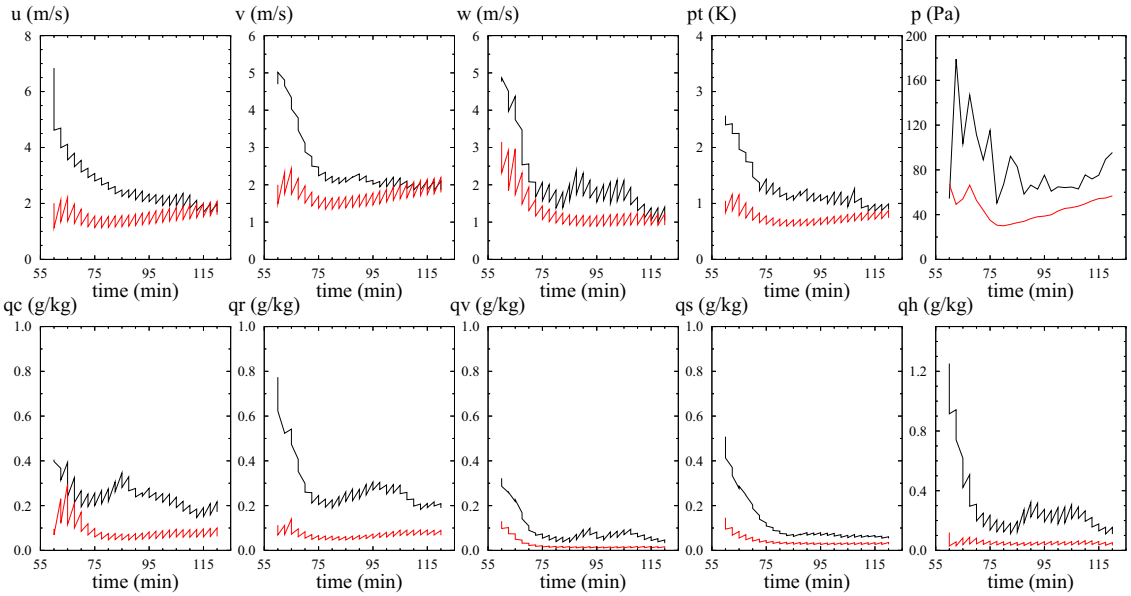

FIG. 9. As in Figure 6, except with 2.5 minute assimilation cycles, higher initial background perturbations, 15% covariance inflation, and a 5 km radius of influence.

over, the radar data are not ingested frequently enough to help the forecast model overcome this problem. The effects of ingesting radar data at smaller time intervals are investigated in Section **4.4**. The increase in RMS error in v, w, q_r and q_h at around 85 minutes is likely due to the interaction of several cells in the truth simulation with the lateral boundaries.

4.4 *EnSRF results with 2.5-minute assimilation cycles*

Certain Distributed Collaborative Adaptive Sensing (DCAS) strategies that will eventually be adopted by the CASA radar network may include full volume scans that will be available every two and a half minutes. The previously described dual-bubble multi-cell case was adapted and re-run, this time outputting data every two and a half minutes; this will examine the effects of assimi-

lating both the CASA and KTLX radar data more frequently and serves as a predecessor to future adaptive DCAS work. The sampled velocity and reflectivity output from the emulators was assimilated into the EnSRF model every two and a half minutes, beginning at one hour (3600 s). As before, only data below three kilometers were used.

Due to the large amount of data that will be ingested into the model every two and a half minutes, covariance inflations of only 10–15% were added to several different model runs. Despite the lower covariance inflation amounts than the five minute assimilation runs, the spread is moderately large enough and the RMS error is comparable (i.e., Figure 9). As before, the horizontal and vertical localization radii were tuned through several trial runs to find the optimal combination of increasing the spread and decreasing the RMS error. The ensemble run with the lowest RMS error had a horizontal and vertical radius of influence of 5 km, smoothed initial perturbations, 15% covariance inflation, and relatively large initial perturbations. The standard deviations of the initial wind field perturbations were 1.5 m s^{-1} for each direction and those of the microphysical variables were 0.0005 g kg^{-1} for each variable. Unlike the previously described five-minute assimilation run that used the same values, the RMS errors were lower than in all previous runs (Figure 9). These reduced errors are likely due to the rapid updates of the model fields by the more frequent radar data ingestion. The slight increase in some of the RMS error plots shown in Figure 9 around 85 minutes is likely due to the interaction of some of the multicell storms with the lateral boundaries. The results of the rapid data assimilation study are very encouraging overall and show great promise for the future inclusion of data from DCAS techniques.

5. SUPERCELL MODEL SIMULATIONS

To compare these multicell system results with a simulated supercell example, a single-bubble supercell simulation based on the 20 May 1977 Del City, Oklahoma event (Ray et al. 1981) is run in the same domain as the multicell simulation. The homogeneous environment is based on the 1500 UTC 20 May 1977 sounding (Figure 10). As before, the physical domain is $96 \times 80 \times 20$ km in the x, y, and z directions, respectively, is centered on the latitude and longitude coordinates (34.7767, -98.0331), and has a horizontal grid spacing of 1.0 km. The 40-layer vertical grid is stretched with a minimum vertical resolution of 200 m at the surface. The numerical truth simulation was initiated in a horizontally homogeneous atmosphere containing an axially symmetric thermal perturbation with a horizontal radius of 10 km and a vertical radius of 1500 m. The temperature is perturbed 4°C at the center (located 1500 m AGL) and decreases gradually to its edge. The warm bubble is initially centered on the point $x = 34$ km, $y = 20$ km. The initial location of the bubble is chosen so that over most of the

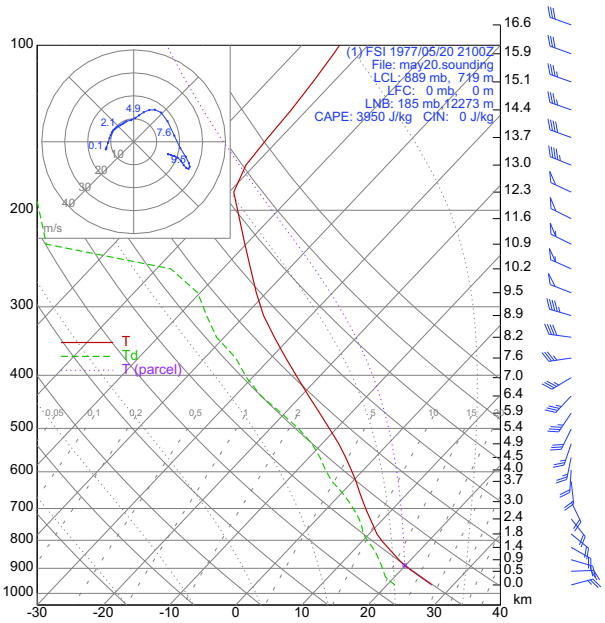

FIG. 10. Skew T-Log P diagram from the 1500 UTC 20 May 1977 KOUN sounding.

assimilation period, the supercell remains within the domain.

Simulated radar data from KTLX and all four CASA radars (under three kilometers) were assimilated into ARPS using the EnSRF technique. Similar to the multicell run described in Section **4.2**, data were first ingested at one hour into the simulation and continued every five minutes for one hour. The horizontal and vertical localization radii were tuned to find the optimal combination that increases the ensemble spread and decreases the RMS error. A covariance inflation of 15% was added to compensate for the small variance that results from the large amount of data ingested. The standard deviations of the initial wind field perturbations were 1.0 m s^{-1} for each direction and those of the microphysical variables were 0.0002 g kg^{-1} for each variable. A smoothing filter was applied to the initially perturbed background state fields. Utilizing a horizontal and vertical radius of influence of six kilometers produced the best RMS error and ensemble spread.

Interestingly, the three-dimensional RMS error values (Figure 11) are higher than the error for the multi-cell simulation (Figure 8), and are much higher than the results of the first test supercell simulations (not shown here) that replicated the work of TX05. These test studies were conducted on a $64 \times 64 \times 16$ km domain with 2 km horizontal and 0.5 km vertical grid spacing (after TX05). These early runs compared the effects of starting the assimilation period at 20 minutes vs. 40 minutes into the truth simulation, which is before the supercell split into two storms and the cold pool had fully developed. The 20-minute 'early start' and 40-minute 'late start' runs had results comparable to those of TX05. The

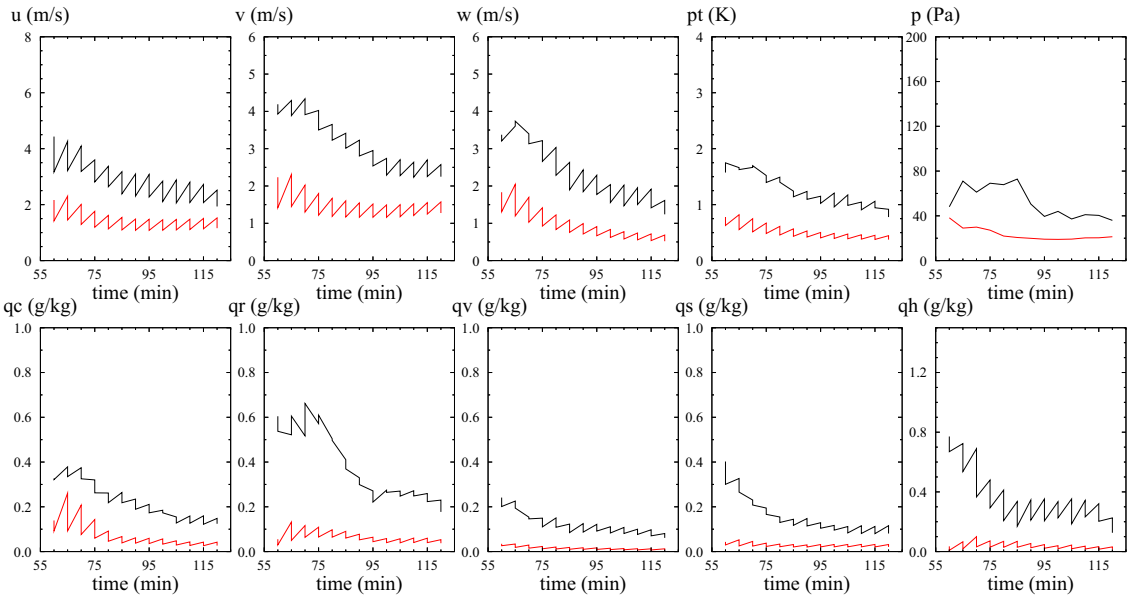

FIG. 11. As in Figure 6, except for the EnSRF supercell simulations and with 15% covariance inflation.

combination of the storm's maturity and complexity at one hour and the fourfold increase in domain resolution most likely account for the higher error in the recent supercell simulation.

To see how much of an effect the later start time has on the model, a sample test run similar to the latest supercell run began assimilating data at 25 minutes and continued for one hour. This test run was similar to the latest supercell run, but used a horizontal radius of influence of 4 km and a vertical influence of 2 km. The three-dimensional RMS error from this simulation is lower (Figure 12), although not as low as the results shown in TX05. Thus, assimilating data at a later time and using a higher-resolution model appears to decrease the ability of ARPS to recreate the simulation.

6. SUMMARY AND DISCUSSION

Significant progress has been made in the last decade in the development of advanced data assimilation methods that are capable of ingesting Doppler radar data in an effort to fully determine the state of the atmosphere. One of these techniques is the ensemble square root Kalman filter (EnSRF), which has shown some success with assimilating real and simulated data from isolated supercell thunderstorms. The effectiveness of the EnSRF technique is not yet understood for other modes of convection such as multicell systems or linear convective systems. More importantly, the effect of adaptive radar data assimilation on numerical weather prediction (NWP) has never been tested.

This project explores the usefulness of adaptive sensing techniques on NWP using a new radar network recently installed in central Oklahoma. The Collaborative Adaptive Sensing of the Atmosphere (CASA) radars can be programmed to scan different portions of the atmosphere adaptively, according to the development of weather systems. Since the radars are not yet operational, the radar data are simulated using observation system simulation experiments (OSSEs). Assimilations and forecasts are performed by incorporating the simulated CASA and WSR-88D radar data into the Advanced Regional Prediction System (ARPS) using the EnSRF method. In this identical-twin experiment, the results of the ensemble mean forecasts are compared with the results of the control simulation. Error is computed for individual state variables, such as wind, potential temperature, pressure, and moisture content.

Preliminary results of EnSRF experiments using simulated data from both KTLX and the four-node CASA network for simulated multicell simulations are promising. Previous work (TX05) has shown that the addition of CASA radar data to that of KTLX improves the overall model performance, and initial results of increased temporal sampling of the multicell simulation also show a decrease in error for most model state variables.

Overall, the supercell simulations are more easily replicated using the EnSRF technique than are the multicell simulations. This is most likely due to the complex and disorganized nature of the multicell system. The initially perturbed background state negatively impacts the various small storms in the unstable multi-cell environment more than the supercell simulations. This is likely due to the weak and transient nature of the individual members of the multicell system, which are not as robust as the isolated supercell. The multicell system also appears to be more sensitive to the adequate capturing of the low-level cold pool because it is more quickly cut

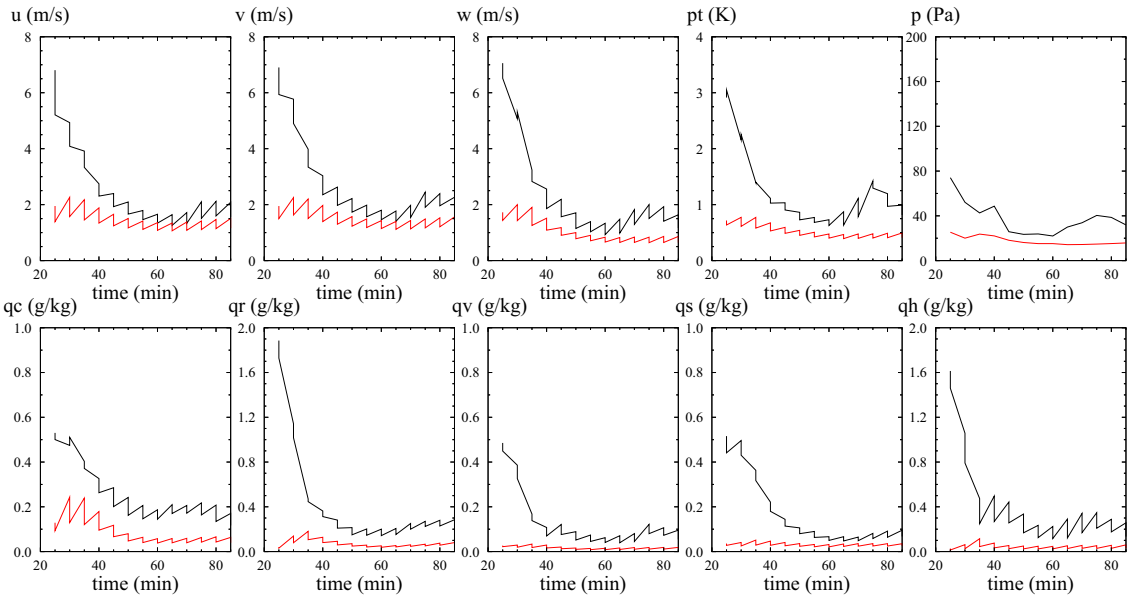

FIG. 12. As in Figure 11, but the assimilation period began at 25 minutes and utilized a smaller radius of influence.

off by a strong cold pool. Additionally, new cells in the multicell system tend to develop on the boundaries of the cold pool and where multiple boundaries intersect, so it is very important for the cold pool of a multicell system to be analyzed correctly.

Multicell systems are complex and difficult to model due to their sensitivity to the initial conditions and model settings. Determining a suitable truth simulation required numerous attempts using different observed and idealized soundings as the background state. Although it took some time to develop this multicell simulation and satisfactory results of the EnSRF simulations, the end result is a multicell example that performs well with the EnSRF technique and will soon be tested using multiple new DCAS strategies. The multicell and supercell trials discussed here can serve as a reference to which the new studies can be compared.

6.1 *Future Work*

The current radar emulator used in this study takes a 'snapshot' of the storm system at one point in time, and it is these data which are assimilated into ARPS. Although convenient, this radar model is not very realistic, and will not be particularly useful for future real-data assimilation cases. One of the unique characteristics and advantages of the CASA system is the ability to scan, on command, different portions of a storm at different levels instead of simply completing full-volume scans. The DCAS abilities were designed into the CASA pedestal, and are meant to eliminate scanning of areas that are unimportant to end users.

Morss et al. (2001) studied adaptive observation sampling strategies with simulated rawinsondes using the 3D-Var technique, and found that these strategies were beneficial for sparse observation networks. The authors also found that the adaptive observations perform best when observations are taken more frequently at fewer locations, and that the adaptive strategy is less effective when observations are taken less frequently. Interestingly, the converse occurred for fixed observation locations (Morss et al. 2001). Although much work has been done on adaptive observation studies (e.g., Lorenz and Emanuel 1998; Hansen and Smith 2000; Emanuel and Langland 1998; Langland et al. 1999b; Szunyogh et al. 2000; Toth et al. 2000; etc...), no work has yet been done on assimilating adaptive radar observations. This is a new area of research that I intend to pursue in the coming year.

Future work will focus on determining the most efficient and cost-effective adaptive scanning strategy for each storm type, along with the necessary sensitivity (i.e., rotation rate) and data ingest rates that are needed for optimal modeling. These idealized numerical simulations will help determine the best model initialization, setup, and scanning strategy for each type of storm system, which will be useful for future real-data assimilation work. If plausible, successful DCAS strategies will be recommended to CASA for future DCAS policy implementation.

Potential work may also include an simulating the effects of assimilating KTLX and CASA radar data of a quasi-linear convective system into ARPS. Studies of different scanning strategies should determine which area of these systems is more important to scan for numerical weather prediction purposes (e.g., the stratiform or convective region or the overall rear-to-front flow structure). Other future work may include an examina-

tion of the importance and effectiveness of an expanded CASA network for forecasting multiple modes of convection will be evaluated.

Acknowledgments. This work was supported primarily by the Engineering Research Centers Program of the National Science Foundation under NSF Award ERC-0228415. Any opinions, findings, and conclusions or recommendations expressed in this material are those of the authors and do not necessarily reflect those of the National Science Foundation.

Future work will be posted online at http://weather.ou.edu/∼savageau/research.

REFERENCES

Anderson, J. L., 1996: A Method for Producing and Evaluating Probabilistic Forecasts from Ensemble Model Integrations. *J. Climate*, **9,** 1518–1530.

Anderson, J. L., 2001: An ensemble adjustment Kalman filter for data assimilation. *Mon. Wea. Rev.*, **129,** 2884–2903.

Arakawa, A. and V. R. Lamb, 1977: Computational design of the basic dynamical processes of the UCLA general circulation model. *Methods in Computational Physics*, **17,** Academic Press, 174–265, 337 pp.

Bishop, C. H., and Z. Toth, 1996: Using ensembles to identify observations likely to improve forecasts. Preprints, *11th Conf. on Numerical Weather Prediction*, Norfolk, VA, Amer. Meteor. Soc., 72–74.

——, B. J. Etherton, and S. J. Majumdar, 2001: Adaptive sampling with the ensemble transform Kalman filter. Part I: theoretical aspects. *Mon. Wea. Rev.*, **129,** 420–436.

Black, T. L., 1994: The new NMC mesoscale Eta model: Description and forecast examples. *Wea. Forecasting*, **9,** 265–278.

Burgers, G., P. J. v. Leeuwen, and G. Evensen, 1998: Analysis scheme in the ensemble Kalman filter. *Mon. Wea. Rev.*, **126,** 1719–1724.

Caya, A., J. Sun, and C. Snyder, 2005: A Comparison between the 4DVAR and the Ensemble Kalman Filter Techniques for Radar Data Assimilation. *Mon. Wea. Rev.*, **133,** 3081–3094.

Charron, M., P. L. Houtekamer, and P. Bartello, 2006: Assimilation with an Ensemble Kalman Filter of Synthetic Radial Wind Data in Anisotropic Turbulence: Perfect Model Experiments. *Mon. Wea. Rev.*, **134,** 618–637.

Chen, C.-S., 1980: The effect of the gust front on the generation of new convection. Ph.D. thesis, University of Illinois, 192 pp.

Droegemeier, K. K. and J. Levit, 1993: The sensitivity of numerically-simulated storm evolution to initial conditions. Preprints, *17th Conf. on Severe Local Storms*, St. Louis, MO, Amer. Meteor. Soc., 431–435.

Dowell, D., F. Zhang, L. J. Wicker, C. Snyder, and N. A. Crook, 2004: Wind and temperature retrievals in the 17 May 1981 Arcadia, Oklahoma supercell: Ensemble Kalman filter experiments. *Mon. Wea. Rev.*, **132,** 1982–2005.

Elmore, K. L., D. J. Stensrud, and K. C. Crawford, 2002: Ensemble cloud model applications to forecasting thunderstorms. *J. Appl. Meteor.*, **41,** 363–383.

——, S. J. Weiss, and P. C. Banacos, 2003: Operational ensemble cloud model forecasts: Some preliminary results. *Wea. Forecasting.*, **18,** 953–964.

Emanuel, K. A., E. N. Lorenz, and R. E. Morss, 1996: Adaptive observations. Preprints, *11th Conf. on Numerical Weather Prediction*, Norfolk, VA, Amer. Meteor. Soc., 67–69.

——, and R. Langland, 1998: FASTEX adaptive observations workshop. *Bull. Amer. Meteor. Soc.*, **79,** 1915–1919.

Evensen, G., 1994: Sequential data assimilation with a nonlinear quasi-geostrophic model using Monte Carlo methods to forecast error statistics. *J. Geophys. Res.*, **99 (C5),** 10,143–10,162.

——, 2003: The ensemble Kalman filter: Theoretical formulation and practical implementation. *Ocean Dynamics*, **53,** 343–367.

Gao, J., M. Xue, Z. Wang, and K. K. Droegemeier, 1998: The initial condition and explicit prediction of convection using ARPS adjoint and other retrieval methods with WSR-88D data. *12th Conf. Num. Wea. Pred.*, Phoenix, AZ, Amer. Meteor. Soc., 176–178.

Hamill, T. M., and S. J. Colluci, 1997a: Evaluation of eta-RSM ensemble probabilistic precipitation forecasts. *Mon. Wea. Rev.*, **125,** 1312–1327.

——, and C. Snyder, 2000: a hybrid ensemble Kalman filter-3D variational analysis scheme. *Mon. Wea. Rev.*, **128,** 2905–2919.

Hansen, J. A., and L. A. Smith, 2000: The role of operational constraints in selecting supplementary observations. *J. Atmos. Sci.* , **57,** 2859–2871.

Houtenkamer, P. L. and H. L. Mitchell, 1998: Data assimilation using an ensemble Kalman filter technique. *Mon. Wea. Rev.*, **126,** 796–811.

——. and ——, 2001: A sequential ensemble Kalman filter for atmospheric data assimilation. *Mon. Wea. Rev.*, **129,** 123–137.

Ide, K. P. Courtier, M. Ghil, and A. Lorenc, 1997: Unified notation for data assimilation: Operational, sequential and variational. *J. Metero. Soc. Japan*, **75,** 181–189.

Janjić, Z. I., 1994: The step-mountain eta coordinate model: Further developments of the convection, viscous sublayer, and turbulence closure schemes. *Mon. Wea. Rev.*, **122,** 927–945.

Jazwinski, A. H., 1970: *Stochastic Processes and Filtering Theory. Academic Press*, 376 pp.

Kain, J. S., S. J. Weiss, D. R. Bright, M. E. Baldwin, M. Dahmer, and J. Levit, 2004: Subjective verification of deterministic models during the 2003 SPC/NSSL Spring Program. *Extended abstract, 20th Conf. Wea. Anal. and For./16th Conf. Num. Wea. Pred.*, Seattle, WA, Amer. Meteor. Soc., 9.3.

——, ——, M. E. Baldwin, G. W. Carbin, D. R. Bright, J. J. Levit, and J. A. Hart, 2005: Evaluating high-resolution configurations of the WRF model that are used to forecast severe convective weather: the 2005 SPC/NSSL Spring Experiment. *Extended abstract, 21st Conf. Wea. Anal. and For./17th Conf. Num. Wea. Pred.*, Washington DC, Amer. Meteor. Soc., 2A.5.

Klemp, J. B., and D. R. Durran, 1983: An upper boundary condition permitting internal gravity wave radiation in numerical mesoscale models. *Mon. Wea. Rev.*, **111,** 430–444.

——, and R. B. Wilhelmson, 1978: The simulation of three-dimensional convective storm dynamics. *J. Atmos. Sci., 35,* 1070–1096.

Kong, F., K. K. Droegemeier, and N. L. Hickmon, 2006a: Multiresolution ensemble forecasts of an observed tornadic thunderstorm system. Part I: Comparison of coarse- and fi ne-grid experiments. *Mon. Wea. Rev., 134,* 807–833.

——, ——, and ——, 2006b: Multiresolution ensemble forecasts of an observed tornadic thunderstorm system. Part II: Storm-scale experiments. *Mon. Wea. Rev.*, accepted.

Langland, R. H., and Coauthors, 1999b: The North Pacific Experiment (NOR-PEX098): Targeted observations for improved North American weather forecasts. *Bull. Amer. Meteor. Soc.*, **80,** 1363–1384.

Leith, C. E., 1974: Theoretical skill of Monte Carlo forecasts. *Mon. Wea. Rev.*, **102,** 409–418.

Lin, Y.-L., R. D. Farley, and H. D. Orville, 1983: Bulk parameterization of the snow field in a cloud model. *J. Climate Appl. Meteor.*, *22,* 1065–1092.

Lorenc, A. C., 1986: Analysis methods for numerical weather prediction. *Quart. J. Roy. Meteor. Soc.*, **112,** 1177–1194.

——, 2003: The potential of the ensemble Kalman filter for NWP–a comparison with 4D-Var. *Quart. J. Roy. Meteor. Soc.*, **129,** 3183–3204.

Lorenz, E. N., 1963: Deterministic nonperiodic flow. *J. Atmos. Sci.*, **20,** 130–141.

——, 1996: Predictability—a problem partly solved. *Proc. ECMWF Seminar on Predictability*. ECMWF, Reading, England, 1–18.

——, and K. A. Emanuel, 1998: Optimal sites for supplementary weather observations: Simulation with a small model. *J. Atmos. Sci.*, **55,** 399–414.

Morss, R. E., K. A. Emanuel, and C. Snyder, 2001: Idealized adaptive observation strategies for improving numerical weather prediction. *J. Atmos. Sci.*, **58,** 210–232.

Nascimento, E. L., and K. K. Droegemeier, 2002: Dynamic adjustment within an idealized numerically-simulated bow echo: implications for data assimilation. *Preprints, Symposium on Observations, Data Assimilation and Probabilistic Prediction*, Orlando, FL, Amer. Meteor. Soc., Orlando, FL, 29–34.

Ray, P. S., B. Johnson, K. W. Johnson, J. S. Bradberry, J. J. Stephens, K. K. Wagner, R. B. Wilhelmson, and J. B. Klemp, 1981: The morphology of severe tornadic storms on 20 May 1977. *J. Atmos. Sci.*, **38,** 1643–1663.

Richardson, Y. P., 1999: The influence of horizontal variations in vertical shear and low-level moisture on numerically simulated convective storms. Ph.D. dissertation, University of Oklahoma, 236 pp.

——, K. K. Droegemeier, and R. P. Davies-Jones, 2006: The Influence of Horizontal Environmental Variability on Numerically-Simulated Convective Storms. Part I: Variations in Vertical Shear. *Mon. Wea. Rev.*, submitted.

Sivillo, J., J. E. Ahlquist, and Z. Toth, 1997: An ensemble forecasting primer. *Wea. Forecasting*, **12,** 809–818.

Smith, P. L., Jr., C. G. Myers, and H. D. Orville, 1975: radar reflectivity factor calculations in numerical cloud models using bulk parameterization of precipitation processes. *J. Appl. Meteor.*, **14,** 1156–1165.

Snyder, C., and F. Zhang, 2003: Assimilation of simulated Doppler radar observations with an ensemble Kalman filter. *Mon. Wea. Rev.*, **131,** 1663–1677.

Sun, J., and N. A. Crook, 1997: Dynamical and microphysical retrieval from Doppler radar observations using a cloud model and its adjoint. Part I: Model development and simulated data experiments. J. Atmos. Sci., 54, 1642-1661.

Szunyogh, I., Z. Toth, K. A. Emanuel, C. Bishop, J. Woolen, T. Marchok, R. Morss, and C. Snyder, 1999: Ensemble-based targeting experiments during FASTEX: The impact of dropsonde data from the Lear jet. *Quart. J. Roy. Meteor. Soc.*, **125,** 3189–3218.

Stull, R. B., 1988: *An Introduction to Boundary Layer Meteorology*. Kluwer Academic, 666 pp.

Tao, W.-K., and J. Simpson, 1993: Goddard cumulus ensemble model. Part I: Model description. *Terres. Atmos. Ocean Sci.*, **4,** 35–72.

Tong, M., and M. Xue, 2005: Ensemble Kalman filter assimilation of Doppler radar data with a compressible nonhydrostatic model: OSS Experiments. *Mon. Wea. Rev.*, **133,** 1789–1807.

——, 2006: Ensemble Kalman Filter Assimilation of Doppler Radar Data for the Initialization and Prediction of Convective Storms. Ph.D. dissertation, University of Oklahoma, 243 pp.

Toth, Z., and Coauthors, 2000: Targeted observations at NCEP: Toward an operational implementation. Preprints, *Fourth Symp. on Integrated Observing Systems*, Long Beach, CA, Amer. Meteor. Soc., 186–193.

Van Den Dool, H. M., and L. Rukhovets, 1994: On the Weights for an Ensemble-Averaged 6–10-Day Forecast. *Wea. Forecasting*, **9,** 457–465.

Weisman, M., and J. Klemp, 1982: The dependence of numerically simulated convective storms on vertical wind shear and buoyancy. *Mon. Wea. Rev.*, **110,** 508–520.

Whitaker, J. S., and T. M. Hamill, 2002: Ensemble data assimilation without perturbed observations. *Mon. Wea. Rev.*, **130,** 1913–1924.

Wobus, R. L., and E. Kalnay, 1995: Three years of operational prediction of forecast skill at NMC. *Mon. Wea. Rev.*, **123,** 2132–2148.

Wood, V. T., and R. A. Brown, 1997: Effects of radar sampling on single-Doppler velocity signatures of mescyclones and tornadoes. *Wea. Forecasting*, **12,** 928–938.

Xue, M., K. K. Droegemeier, and V. Wong, 2000: The Advanced Regional Prediction System (ARPS) - A multiscale nonhydrostatic atmospheric simulation and prediction tool. Part I: Model dynamics and verification. *Meteor. Atmos. Physics*, **75,** 161–193.

——, ——, ——, A. Shapiro, K. Brewster, F. Carr, D. Weber, Y. Liu, and D.-H. Wang, 2001: The Advanced Regional Prediction System (ARPS) - A multiscale nonhydrostatic atmospheric simulation and prediction tool. Part II: Model physics and applications. *Meteor. Atmos. Phy.*, **76,** 143–165.

——, D.-H. Wang, J.-D. Gao, K. Brewster, and K. K. Droegemeier, 2003: The Advanced Regional Prediction System (ARPS), storm-scale numerical weather prediction and data asimilation. *Meteor. Atmos. Physics*, **82,** 139–170.

——, M. Tong, and K. K. Droegemeier, 2006: An OSSE Framework Based on the Ensemble Square Root Kalman Filter for Evaluating the Impact of Data from Radar Networks on Thunderstorm Analysis and Forecasting. *J. Atmos. Oceanic Tech.*, **23,** 46–66.

Zhang, F., C. Snyder, and J. Sun, 2004: Impacts of initial estimate and observations on the convective-scale data assimilation with an ensemble Kalman filter. *Mon. Wea. Rev.*, **132,** 1238–1253.

Zhu, Y., G. Iyengar, Z. Toth, M. S. Tracton, and T. Marchok, 1996: Objective evaluation of the NCEP global ensemble forecasting system. Preprints, *11th Conf. on Numerical Weather Prediction*, Norfolk, VA, Amer. Meteor. Soc., 79J–82J.